THE JOURNAL OF PHYSICAL CHEMISTRY Letters

Letter

pubs.acs.org/JPCL

Dynamics of Electron Injection in SnO_2/TiO_2 Core/Shell Electrodes for Water-Splitting Dye-Sensitized Photoelectrochemical Cells

Nicholas S. McCool,[†] John R. Swierk,[∥] Coleen T. Nemes,[∥] Charles A. Schmuttenmaer,*[,∥] and Thomas E. Mallouk*[,†,‡,§]

[†]Department of Chemistry, [‡]Department of Biochemistry and Molecular Biology, and [§]Department of Physics, The Pennsylvania State University, University Park, Pennsylvania 16802, United States

[∥]Department of Chemistry and Energy Sciences Institute, Yale University, 225 Prospect Street, P.O. Box 208107, New Haven, Connecticut 06520-8107, United States

Supporting Information

ABSTRACT: Water-splitting dye-sensitized photoelectrochemical cells (WS-DSPECs) rely on photoinduced charge separation at a dye/semiconductor interface to supply electrons and holes for water splitting. To improve the efficiency of charge separation and reduce charge recombination in these devices, it is possible to use core/shell structures in which photoinduced electron transfer occurs stepwise through a series of progressively more positive acceptor states. Here, we use steady-state emission studies and time-resolved terahertz spectroscopy to follow the dynamics of electron injection from a photoexcited ruthenium polypyridyl dye as a function of the TiO_2 shell thickness on SnO_2 nanoparticles. Electron injection proceeds directly into the SnO_2 core when the thickness of the TiO_2 shell is less than 5 Å. For thicker shells, electrons are injected into the TiO_2 shell and trapped, and are then released into the SnO_2 core on a time scale of hundreds of picoseconds. As the TiO_2 shell increases in thickness, the probability of electron trapping in nonmobile states within the shell increases. Conduction band electrons in the TiO_2 shell and the SnO_2 core can be differentiated on the basis of their mobility. These observations help explain the observation of an optimum shell thickness for core/shell water-splitting electrodes.

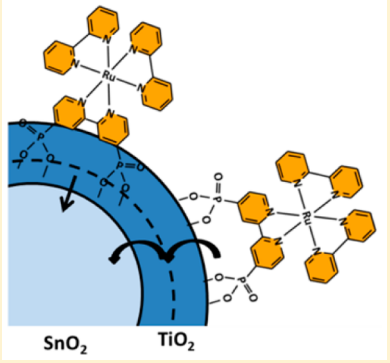

Harnessing and converting solar energy into a useful form, for example, electricity or a chemical fuel, on a terawatt scale is among the most critical scientific challenges of the 21st century.[1] Natural photosynthesis does so, but with inherent efficiency limitations that can be surpassed in artificial systems.[2] In natural photosynthesis, a hierarchical assembly of light harvesting pigments funnel excitation energy into a reaction center, where a series of subnanosecond electron transfers occurs to yield a charge separated state with nearly 100% quantum efficiency.[3−5] Efficient charge transfer in natural photosynthesis relies on an optimized electron transfer cascade between the various donor and acceptor species. Achieving the same level of control over electron transfer events is a central goal of artificial photosynthesis, which seeks to develop artificial systems capable of using solar energy to photocatalytically drive water splitting and other fuel-forming endergonic reactions.[6−8]

Water-splitting dye-sensitized photoelectrochemical cells (WS-DSPECs) accomplish artificial photosynthesis by utilizing a semiconducting metal oxide film-sensitized with a molecular dye, which absorbs visible light and injects an electron into the oxide semiconductor. Holes diffuse across the surface via a series of lateral electron transfer events between dye molecules until they arrive at a catalytic site. This process repeats until the catalyst collects enough holes to oxidize water, generating molecular oxygen and four protons. The injected electrons diffuse through the electrode to a transparent conductive oxide electrode and ultimately to a dark cathode where protons are reduced to hydrogen.[9]

Unfortunately, the quantum efficiencies of WS-DSPECs are only a few percent because hole transport and catalytic water oxidation are slow.[10] As a result, rapid recombination between the injected electron and the oxidized dye is the dominant mechanism for efficiency loss in these devices.[11] The use of visible light-absorbing dyes that are sufficiently oxidizing to drive water oxidation near neutral pH results in low injection yields into anatase TiO_2 (η_{inj} = 20−30%).[11−13] As an alternative, research on WS-DSPECs has focused on using SnO_2 as the electrode material.[14,15] SnO_2 has a conduction band minimum (CBM) several hundred millivolts below that of TiO_2,[13,16,17] leading to improved injection yields.[13] The more positive CBM of SnO_2 also lowers the driving force for recombination. However, the rate of recombination has been found to be much faster for SnO_2 than for TiO_2 electrodes.[17,18]

One strategy for slowing down recombination while maintaining efficient injection is the use of a core/shell electrode architecture.[19] Recent work by Meyer and co-workers demonstrated a SnO_2/TiO_2 core/shell structure prepared by atomic layer deposition (ALD) of TiO_2 on SnO_2 nanoparticles.

Received: July 13, 2016
Accepted: July 14, 2016
Published: July 14, 2016

DOI: 10.1021/acs.jpclett.6b01528
J. Phys. Chem. Lett. 2016, 7, 2930−2934

This architecture results in an electron transfer cascade from the dye excited state into TiO_2 and subsequently into the SnO_2 CB, as shown in Scheme 1.[14,15] They observed efficient

Scheme 1. Energy Diagram for the SnO_2/TiO_2 Structure and Structure of Ru(II)Phos[a]

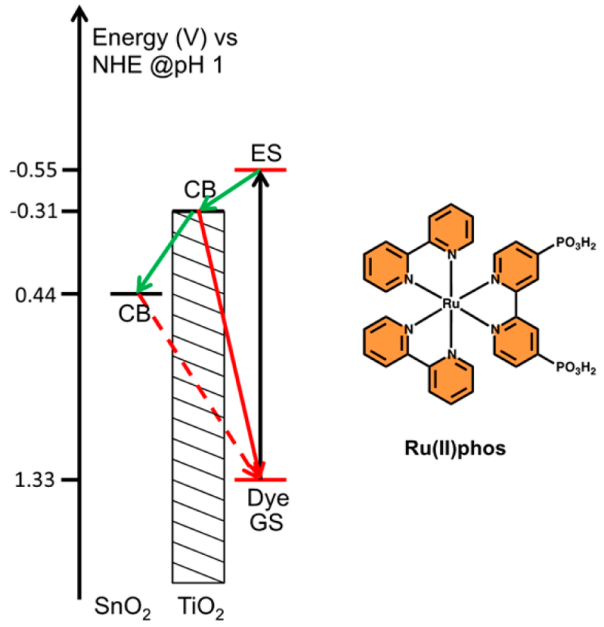

[a]Potentials for ES and GS of Ru(II)phos taken from ref 21; for oxide, CBM taken from ref 16.

electron injection, slower recombination kinetics, and an overall enhancement in device performance. Knauf et al.[20] explored recombination with TiO_2 shells of varying thickness on SnO_2 and ZrO_2. Interestingly, they found that for shells thicker than 3.5 nm, electron recombination originated from localized electrons in the TiO_2 shell, whereas for thinner shells recombination proceeded via a tunneling mechanism. Recently, we studied the ultrafast injection dynamics of sensitized bare-SnO_2 and SnO_2 coated with 2.5 nm of TiO_2 using time-resolved terahertz spectroscopy (TRTS).[13] In that study, we demonstrated that addition of the TiO_2 markedly changed the injection kinetics. We suggested that an initial ultrafast injection component not apparent with bare SnO_2 demonstrated injection into the TiO_2 shell, followed by fast trapping and subsequent electron release into SnO_2 on a much longer time scale. In this study, we revisit that system and use TRTS and steady state emission measurements to probe the electron injection process as a function of shell thickness.

Details of sample preparation are available in Supporting Information. Briefly, we utilized atomic layer deposition (ALD) to prepare TiO_2 shells of varying thickness on mesoporous SnO_2. ALD is a well-established technique for the deposition of conformal, atomically thin films of metal oxides on surfaces and has been used with great success in mesoporous structures.[22,23] Our previous work deposited 40 cycles of TiO_2 on SnO_2, resulting in a film thickness of 2.5 nm as measured by deposition on a Si wafer.[13] This normalization infers a deposition of about 0.63 Å per cycle. In order to gain a better understanding of when shell material impacted charge injection, we varied the shell thickness from 1 to 40 pulse cycles, or a nominal thickness range of submonolayer coverage up to 2.5 nm. This deposition process was also carried out on porous nanocrystalline ZrO_2 films in order to probe how effectively the TiO_2 shell alone with varying thicknesses could accept electrons from the dye.

Figure 1 shows the peak emission for both SnO_2/TiO_2 and ZrO_2/TiO_2 core/shell structures sensitized with bis(2,2-bipyridine)(4,4-diphosphonato-2,2-bipyridine)ruthenium(II) bromide (Ru(II)phos) at pH 1. Because both SnO_2 and TiO_2 accept electrons from the excited state of the dye, we anticipated significant emission quenching from injection into the SnO_2/TiO_2 architecture at all thicknesses of TiO_2, as can be seen in Figure 1 (red squares). In the case of the ZrO_2/TiO_2 samples, the ZrO_2 core has a CBM well above the excited state potential of the dye and should not be able to quench the excited state of the dye. This can be seen in Figure 1 (blue circles) where there is significant emission intensity when the TiO_2 shell is thin. With thicker TiO_2 shells, the emission intensity decreases until ~13 Å of TiO_2, after which it is similar to SnO_2/TiO_2. The complete quenching of the excited state demonstrates that at ≥10 Å of TiO_2, electron cascade through the shell completely controls the injection kinetics. Furthermore, the lack of emission quenching suggests that for shell thicknesses below ~2 Å tunneling through the TiO_2 dominates.[24] At intermediate thicknesses, a combination of tunneling and electron cascade may be occurring. In this size regime, quantum confinement effects can occur, resulting in an increase in the band gap and a shift of the CBM to more negative potentials.[25]

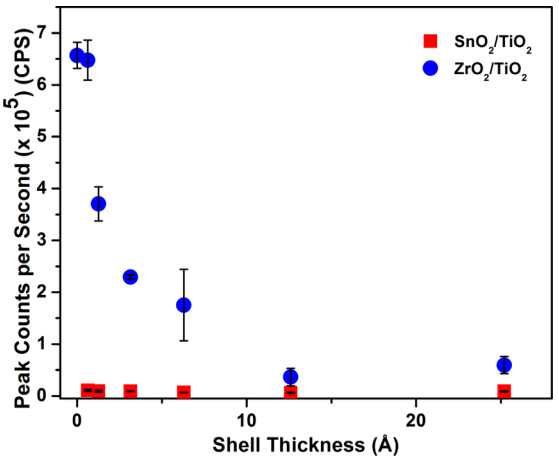

Figure 1. Peak emission intensity between 510 and 800 nm measured from Ru(II)phos-sensitized core/shell films with varying thicknesses of the TiO_2 shell on a SnO_2 core (red squares) and a ZrO_2 core (blue circles). Emission was measured in N_2-purged, 0.1 M $HClO_4$ (pH 1) aqueous solution.

We can gain insight into the dynamics of injection by monitoring the ultrafast injection kinetics. Despite having a lower CBM energy (and as a result, a higher driving force for injection and lower driving force for recombination), SnO_2 exhibits slow injection dynamics[13,26,27] when compared to TiO_2. The slow injection kinetics are a result of a low density of states (DOS) in the SnO_2 CB,[26] which is comprised primarily of Sn^{4+} s and p orbitals,[26] whereas TiO_2 has a high CB DOS made of Ti^{4+} d orbitals.[28,29] To understand the effect of TiO_2 shell thickness on injection, we utilized TRTS, which is an ultrafast, far-infrared technique that is sensitive to changes in conductivity.[13,30−33] Electrons injected into mobile states (e.g., the conduction band) attenuate transmitted terahertz (THz)

DOI: 10.1021/acs.jpclett.6b01528
J. Phys. Chem. Lett. 2016, 7, 2930−2934

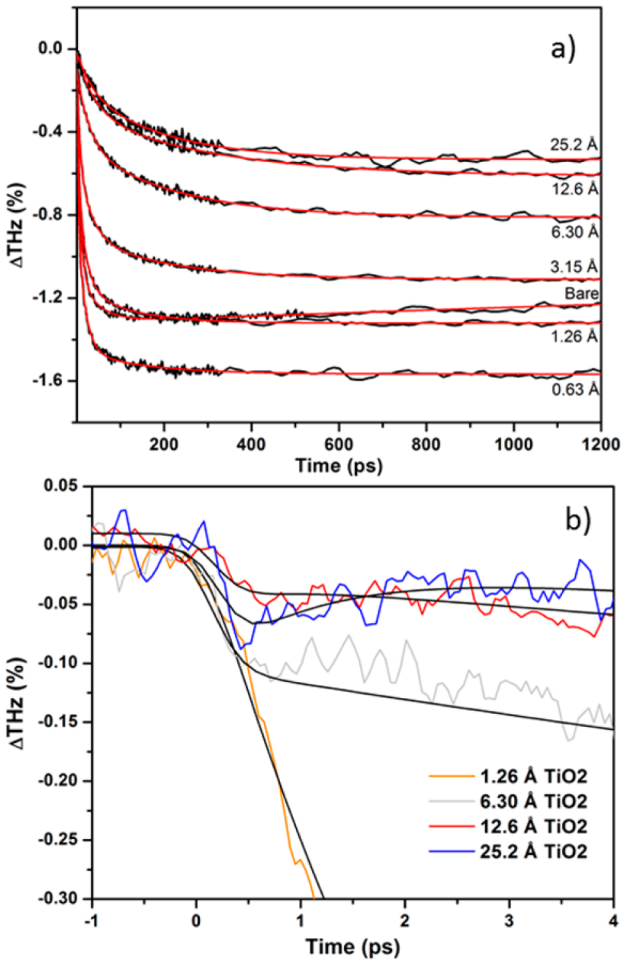

Figure 2. (a) Long time scale time-resolved THz spectroscopy (TRTS) traces for SnO_2/TiO_2 electrodes with varying shell thicknesses. (b) Short time scale plot of the TRTS traces of a collection of samples from (a) in order to show the evolution of the initial injection into the TiO_2 shell with increasing thickness. TRTS scans were collected in a 0.1 M pH 1 $HClO_4$ aqueous solution.

radiation such that increases in conductivity following injection are observed as a decrease in the transmitted THz amplitude. Additionally, because the conductivity change depends in part on the electron mobility, TRTS is ideally suited for distinguishing whether the electron is located in the TiO_2-shell or SnO_2-core on the basis of the difference in electron mobility between the two materials.

Figure 2 shows the TRTS traces (black) and respective fits (red) using eq 1:

$$\Delta THz\left\{\Delta THz_0 + \sum_{i=1}^{n} A_i\left[\exp\left(-\frac{t-t_0}{\tau_i}\right) - 1\right]\right\} \otimes G(FWHM) \quad (1)$$

where ΔTHz_0 is the baseline before $t = 0$, n is the number of exponentials included in the fit, t_0 corresponds to the injection time (i.e., $t = 0$), A_i is the amplitude of a given component, τ_i is the lifetime of a given component, G(fwhm) is a Gaussian instrument response function (determined to be 0.5 ps) and $\otimes$ represents a convolution. Full fitting parameters are summarized in Table S1. The injection component of all traces from bare SnO_2 to 6 Å of TiO_2 were successfully fit using a three exponential equation, though slow trapping dynamics observed in the bare samples required a fourth exponential (with a negative amplitude to represent trapping) to be included in the fit. Films coated with 12.5 and 25 Å required a fourth exponential to accurately reproduce trapping which occurs in the initial (0−5 ps) dynamics.

Surprisingly, we observe a higher THz attenuation for samples coated with 0.63 and 1.26 Å of TiO_2 when compared to bare SnO_2, corresponding to a higher density of mobile electrons in the SnO_2 film. In order to ensure that changes in THz attenuation with shell thickness are not a result of different dye loading (e.g., a lower dye loading due to blocked pores), UV/vis spectra were measured for all samples. A summary of dye loading is shown in Figure S1, which demonstrates that loading across all samples is nearly within experimental error of each other. In fact, thicker shells show slightly increased dye loading, and would therefore not be expected to show diminished injection amplitude based on dye loading alone. As the dye loading is nearly identical between these samples, we suggest that the increase in injection amplitude is related to passivation of nonmobile surface states. These nonmobile states are generally ascribed to uncoordinated metal centers and can act as acceptors states for charge injection and, as a result, will not be observed with TRTS. The process of injection into nonmobile surface states in aqueous electrolyte has been observed by others using sensitized ZnO[34,35] as well as in our previous work focused on proton-induced surface trap states, which also detailed the inability of TRTS to observe these electrons.[36] The passivation of these states is further supported by the lack of slow trapping in any of the ALD coated samples when compared to the bare SnO_2. The slow decay in the TRTS trace for bare SnO_2 is suggestive of trapping into surface states, as none of the TiO_2-coated samples exhibit any long time, slow loss of THz amplitude associated with trapping. Hupp and co-workers observed a similar passivation of surface states with ALD.[24]

The dynamics observed for the 25 Å sample agree very well with our previous report on this system.[13] In that report, we assigned the rapid (<0.5 ps) decrease and recovery of the THz amplitude from 0 to 5 ps as rapid injection into TiO_2 followed by trapping within the TiO_2 or at the TiO_2/SnO_2 interface (Figure 2b), with release into the SnO_2 core at longer time scales. We can clearly distinguish an evolving ultrafast injection component for samples with a TiO_2 shell of 6 Å or more, which strongly suggests that electrons are injecting directly into the TiO_2 shell. By comparing the initial injection lifetime, injection shifts with increasing shell thickness from occurring with a lifetime of several picoseconds to being instrument limited at <0.5 ps, which is consistent with injection into TiO_2 being much faster than into SnO_2. This is attributed to a higher DOS in the TiO_2 CB than in SnO_2 as described above.[13] A fast trapping component can be clearly distinguished with increasing shell thickness (Figure 2b), suggesting that the trapping sites are located in the TiO_2 shell and not at the SnO_2/TiO_2 interface. This is also consistent with work by Knauf et al., who directly observed the recombination rate of electrons with oxidized Ru(II)phos in SnO_2/TiO_2 structures and found that beyond a few nanometers, recombination occurs entirely from the TiO_2 shell.[20] As we noted in our previous work, after injection into the TiO_2 shell, the release kinetics from the shell into the core material are largely independent of shell thickness.[13]

Figure 3 shows the scaling factor and electron transfer rate, $1/\langle\tau_w\rangle$, where τ_w is a weighted average of the injection lifetimes,

DOI: 10.1021/acs.jpclett.6b01528
J. Phys. Chem. Lett. 2016, 7, 2930−2934

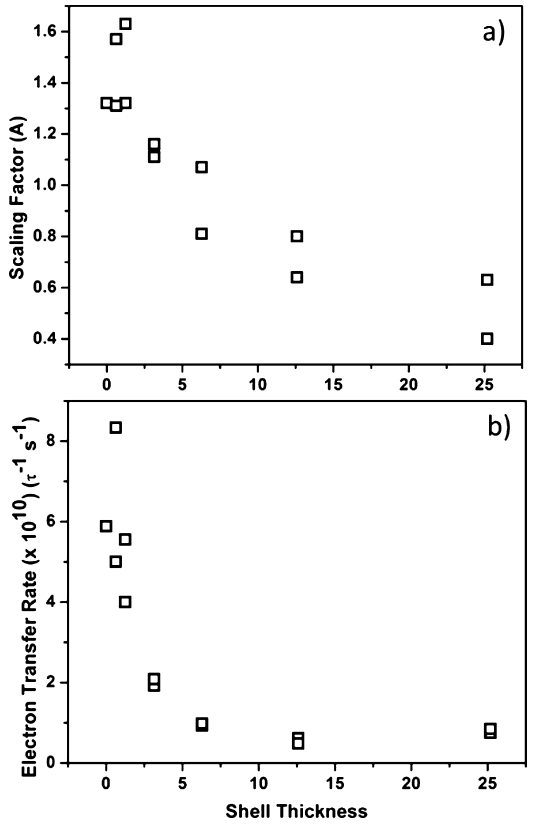

Figure 3. (a) Scaling factor and (b) weighted rate of electron transfer from fits to TRTS traces in Figure 2 for varying shell thicknesses.

as a function of shell thickness (Table S1). The scaling factor represents the overall injection yield of each trace and is a sum of the *A* components before normalization for each trace; the value is included in Table S1. This factor is directly proportional to the number of mobile electrons and thus by extension to the injection amplitude. Interestingly, we find that the rate of electron transfer becomes largely constant after approximately 5 Å of TiO_2, which is consistent with steady state emission data for sensitized TiO_2/ZrO_2. This suggests that after 5 Å the excited state of the dye "senses" only the TiO_2 shell. It is surprising then that we do not also see a leveling of the scaling factor. One likely explanation is that as the TiO_2 shell increases in thickness more electrons are injected directly into nonmobile sites and therefore are invisible to TRTS. These electrons can directly recombine with oxidized dye molecules on the surface. The increase in trapping within the shell with increasing shell thickness observed in Figure 2b supports that hypothesis.

Though TRTS has been used to probe core/shell nanostructures,[37,38] this and our previous study[13] are the first to explicitly follow the movement of an electron through the shell and into the core, demonstrating the power of TRTS for these types of architectures. By varying the thickness of the TiO_2 shell, we were able to demonstrate that electron injection proceeds directly into the SnO_2 core when the TiO_2 shell is less than 5 Å, but when the thickness is greater than 5 Å, it is injected first into the TiO_2 shell and then moves to the SnO_2 core. Furthermore, we were able to demonstrate that trapping of carriers into nonmobile sites occurs specifically within the TiO_2 shell. The degree of trapping in the shell increases with increasing shell thickness, further demonstrating the need to balance injection and recombination dynamics through an optimal shell thickness.

■ ASSOCIATED CONTENT

Supporting Information

The Supporting Information is available free of charge on the ACS Publications website at DOI: 10.1021/acs.jpclett.6b01528.

Experimental details, fitting parameters for TRTS traces, and UV/vis data for dye surface coverage. (PDF)

■ AUTHOR INFORMATION

Corresponding Authors

*E-mail: charles.schmuttenmaer@yale.edu. Phone: (203) 432-3915.

*E-mail: tem5@psu.edu. Phone: (814) 863-9637.

Notes

The authors declare no competing financial interest.

■ ACKNOWLEDGMENTS

We thank Svante Hedström for his suggestions during the preparation of the manuscript. This work was supported by the Office of Basic Energy Sciences, Division of Chemical Sciences, Geosciences, and Energy Biosciences, Department of Energy, under contracts DE-FG02-07ER15911 and DE-FG02-07ER15909 as well as by a generous donation from the TomKat Charitable Trust. N.S.M. thanks the National Science Foundation for support as a graduate fellow under Grant DGE1255832. Instrumentation and facilities used in this project were supported by the Pennsylvania State University Materials Research Institute Nanofabrication Laboratory under National Science Foundation Cooperative Agreement ECS-0335765.

■ REFERENCES

(1) Lewis, N. S.; Nocera, D. G. Powering the Planet: Chemical Challenges in Solar Energy Utilization. *Proc. Natl. Acad. Sci. U. S. A.* **2006**, *103* (43), 15729−15735.

(2) Nealson, K. H.; Conrad, P. G. Life: Past, Present and Future. *Philos. Trans. R. Soc., B* **1999**, *354* (1392), 1923−1939.

(3) Moore, G. F.; Brudvig, G. W. Energy Conversion in Photosynthesis: A Paradigm for Solar Fuel Production. *Annu. Rev. Condens. Matter Phys.* **2011**, *2* (1), 303−327.

(4) Blankenship, R. E.; Tiede, D. M.; Barber, J.; Brudvig, G. W.; Fleming, G.; Ghirardi, M.; Gunner, M. R.; Junge, W.; Kramer, D. M.; Melis, A.; et al. Comparing Photosynthetic and Photovoltaic Efficiencies and Recognizing the Potential for Improvement. *Science* **2011**, *332* (6031), 805−809.

(5) Grabolle, M.; Dau, H. Energetics of Primary and Secondary Electron Transfer in Photosystem II Membrane Particles of Spinach Revisited on Basis of Recombination-Fluorescence Measurements. *Biochim. Biophys. Acta, Bioenerg.* **2005**, *1708* (2), 209−218.

(6) Gust, D.; Moore, T. A.; Moore, A. L. Solar Fuels via Artificial Photosynthesis. *Acc. Chem. Res.* **2009**, *42* (12), 1890−1898.

(7) Wasielewski, M. R. Self-Assembly Strategies for Integrating Light Harvesting and Charge Separation in Artificial Photosynthetic Systems. *Acc. Chem. Res.* **2009**, *42* (12), 1910−1921.

(8) Kärkäs, M. D.; Johnston, E. V.; Verho, O.; Åkermark, B. Artificial Photosynthesis: From Nanosecond Electron Transfer to Catalytic Water Oxidation. *Acc. Chem. Res.* **2014**, *47* (1), 100−111.

(9) Swierk, J. R.; Mallouk, T. E. Design and Development of Photoanodes for Water-Splitting Dye-Sensitized Photoelectrochemical Cells. *Chem. Soc. Rev.* **2013**, *42* (6), 2357−2387.

(10) Zhao, Y.; Swierk, J. R.; Megiatto, J. D.; Sherman, B.; Youngblood, W. J.; Qin, D.; Lentz, D. M.; Moore, A. L.; Moore, T.

DOI: 10.1021/acs.jpclett.6b01528
J. Phys. Chem. Lett. 2016, 7, 2930−2934

A.; Gust, D.; et al. Improving the Efficiency of Water Splitting in Dye-Sensitized Solar Cells by Using a Biomimetic Electron Transfer Mediator. *Proc. Natl. Acad. Sci. U. S. A.* **2012**, *109* (39), 15612−15616.
(11) Swierk, J. R.; McCool, N. S.; Mallouk, T. E. Dynamics of Electron Recombination and Transport in Water-Splitting Dye-Sensitized Photoanodes. *J. Phys. Chem. C* **2015**, *119* (24), 13858−13867.
(12) Swierk, J. R.; Méndez-Hernández, D. D.; McCool, N. S.; Liddell, P.; Terazono, Y.; Pahk, I.; Tomlin, J. J.; Oster, N. V.; Moore, T. A.; Moore, A. L.; et al. Metal-Free Organic Sensitizers for Use in Water-Splitting Dye-Sensitized Photoelectrochemical Cells. *Proc. Natl. Acad. Sci. U. S. A.* **2015**, *112* (6), 1681−1686.
(13) Swierk, J. R.; McCool, N. S.; Nemes, C. T.; Mallouk, T. E.; Schmuttenmaer, C. A. Ultrafast Electron Injection Dynamics of Photoanodes for Water-Splitting Dye-Sensitized Photoelectrochemical Cells. *J. Phys. Chem. C* **2016**, *120* (11), 5940−5948.
(14) Wee, K.-R.; Sherman, B. D.; Brennaman, M. K.; Sheridan, M. V.; Nayak, A.; Alibabaei, L.; Meyer, T. J. An Aqueous, Organic Dye Derivatized SnO_2/TiO_2 Core/shell Photoanode. *J. Mater. Chem. A* **2016**, *4* (8), 2969−2975.
(15) Sherman, B. D.; Ashford, D. L.; Lapides, A. M.; Sheridan, M. V.; Wee, K. R.; Meyer, T. J. Light-Driven Water Splitting with a Molecular Electroassembly-Based Core/Shell Photoanode. *J. Phys. Chem. Lett.* **2015**, *6* (16), 3213−3217.
(16) Grätzel, M. Photoelectrochemical Cells. *Nature* **2001**, *414* (6861), 338−344.
(17) Green, A. N. M.; Palomares, E.; Haque, S. A.; Kroon, J. M.; Durrant, J. R. Charge Transport versus Recombination in Dye-Sensitized Solar Cells Employing Nanocrystalline TiO_2 and SnO_2 Films. *J. Phys. Chem. B* **2005**, *109* (25), 12525−12533.
(18) Kamat, P. V.; Bedja, I.; Hotchandani, S.; Patterson, L. K. Photosensitization of Nanocrystalline Semiconductor Films. Modulation of Electron Transfer between Excited Ruthenium Complex and SnO_2 Nanocrystallites with an Externally Applied Bias. *J. Phys. Chem.* **1996**, *100* (12), 4900−4908.
(19) Lee, S. A.; Zhao, Y.; Hernandez-Pagan, E. A.; Blasdel, L.; Youngblood, W. J.; Mallouk, T. E. Electron Transfer Kinetics in Water Splitting Dye-Sensitized Solar Cells Based on Core−shell Oxide Electrodes. *Faraday Discuss.* **2012**, *155*, 165−179.
(20) Knauf, R. R.; Kalanyan, B.; Parsons, G. N.; Dempsey, J. L. Charge Recombination Dynamics in Sensitized SnO_2/TiO_2 Core/Shell Photoanodes. *J. Phys. Chem. C* **2015**, *119* (51), 28353−28360.
(21) Hanson, K.; Brennaman, M. K.; Ito, A.; Luo, H.; Song, W.; Parker, K. A.; Ghosh, R.; Norris, M. R.; Glasson, C. R. K.; Concepcion, J. J.; et al. Structure−Property Relationships in Phosphonate-Derivatized, Ru II Polypyridyl Dyes on Metal Oxide Surfaces in an Aqueous Environment. *J. Phys. Chem. C* **2012**, *116* (28), 14837−14847.
(22) Dendooven, J.; Devloo-Casier, K.; Levrau, E.; Van Hove, R.; Sree, S. P.; Baklanov, M. R.; Martens, J. A.; Detavernier, C. In Situ Monitoring of Atomic Layer Deposition in Nanoporous Thin Films Using Ellipsometric Porosimetry. *Langmuir* **2012**, *28* (8), 3852−3859.
(23) Johnson, R. W.; Hultqvist, A.; Bent, S. F. A Brief Review of Atomic Layer Deposition: From Fundamentals to Applications. *Mater. Today* **2014**, *17* (5), 236−246.
(24) Prasittichai, C.; Avila, J. R.; Farha, O. K.; Hupp, J. T. Systematic Modulation of Quantum (Electron) Tunneling Behavior by Atomic Layer Deposition on Nanoparticulate SnO_2 and TiO_2 Photoanodes. *J. Am. Chem. Soc.* **2013**, *135* (44), 16328−16331.
(25) Sakai, N.; Ebina, Y.; Takada, K.; Sasaki, T. Electronic Band Structure of Titania Semiconductor Nanosheets Revealed by Electrochemical and Photoelectrochemical Studies. *J. Am. Chem. Soc.* **2004**, *126* (18), 5851−5858.
(26) Ai, X.; Anderson, N. A.; Guo, J.; Lian, T. Electron Injection Dynamics of Ru Polypyridyl Complexes on SnO2 Nanocrystalline Thin Films. *J. Phys. Chem. B* **2005**, *109* (15), 7088−7094.
(27) Benkö, G.; Myllyperkio, P.; Pan, J.; Yartsev, A. P.; Sundstrom, V. Photoinduced Electron Injection from Ru(dcbpy)2(NCS)2 to SnO2 and TiO2 Nanocrystalline Films. *J. Am. Chem. Soc.* **2003**, *125*, 1118−1119.
(28) Anderson, N. A.; Ai, X.; Lian, T. Electron Injection Dynamics from Ru Polypyridyl Complexes to ZnO Nanocrystalline Thin Films. *J. Phys. Chem. B* **2003**, *107* (51), 14414−14421.
(29) Sorantin, P.; Schwarz, K. Chemical Bonding in Rutile-Type Compounds. *Inorg. Chem.* **1992**, *31* (17), 567−576.
(30) Beard, M. C.; Turner, G. M.; Schmuttenmaer, C. A. Transient Photoconductivity in GaAs as Measured by Time-Resolved Terahertz Spectroscopy. *Phys. Rev. B: Condens. Matter Mater. Phys.* **2000**, *62* (23), 15764−15777.
(31) Turner, G. M.; Beard, M. C.; Schmuttenmaer, C. A. Carrier Localization and Cooling in Dye-Sensitized Nanocrystalline Titanium Dioxide. *J. Phys. Chem. B* **2002**, *106* (45), 11716−11719.
(32) Baxter, J. B.; Schmuttenmaer, C. A. Conductivity of ZnO Nanowires, Nanoparticles, and Thin Films Using Time-Resolved Terahertz Spectroscopy. *J. Phys. Chem. B* **2006**, *110* (50), 25229−25239.
(33) Nemes, C. T.; Koenigsmann, C.; Schmuttenmaer, C. A. Functioning Photoelectrochemical Devices Studied with Time-Resolved Terahertz Spectroscopy. *J. Phys. Chem. Lett.* **2015**, *6* (16), 3257−3262.
(34) Furube, A.; Katoh, R.; Hara, K.; Murata, S.; Arakawa, H.; Tachiya, M. Ultrafast Stepwise Electron Injection from Photoexcited Ru-Complex into Nanocrystalline ZnO Film via Intermediates at the Surface. *J. Phys. Chem. B* **2003**, *107* (17), 4162−4166.
(35) Furube, A.; Katoh, R.; Yoshihara, T.; Hara, K.; Murata, S.; Arakawa, H.; Tachiya, M. Ultrafast Direct and Indirect Electron-Injection Processes in a Photoexcited Dye-Sensitized Nanocrystalline Zinc Oxide Film: The Importance of Exciplex Intermediates at the Surface. *J. Phys. Chem. B* **2004**, *108* (33), 12583−12592.
(36) McCool, N. S.; Swierk, J. R.; Nemes, C. T.; Saunders, T. P.; Schmuttenmaer, C. A.; Mallouk, T. E. Proton-Induced Trap States, Injection and Recombination Dynamics in Water-Splitting Dye-Sensitized Photoelectrochemical Cells. *ACS Appl. Mater. Interfaces* **2016**, *8* (26), 16727−16735.
(37) Parkinson, P.; Joyce, H. J.; Gao, Q.; Tan, H. H.; Zhang, X.; Zou, J.; Jagadish, C.; Herz, L. M.; Johnston, M. B. Carrier Lifetime and Mobility Enhancement in Nearly Defect-Free Core−Shell Nanowires Measured Using Time-Resolved Terahertz Spectroscopy. *Nano Lett.* **2009**, *9* (9), 3349−3353.
(38) Boland, J. L.; Casadei, A.; Tütüncüoglu, G.; Matteini, F.; Davies, C. L.; Jabeen, F.; Joyce, H. J.; Herz, L. M.; Fontcuberta i Morral, A.; Johnston, M. B. Increased Photoconductivity Lifetime in GaAs Nanowires by Controlled N-Type and P-Type Doping. *ACS Nano* **2016**, *10* (4), 4219−4227.

DOI: 10.1021/acs.jpclett.6b01528
J. Phys. Chem. Lett. 2016, 7, 2930−2934

Supporting Information for: Dynamics of Electron Injection in SnO_2/TiO_2 Core/Shell Electrodes for Water-splitting Dye-Sensitized Photoelectrochemical Cells

Nicholas S. McCool,[1] John R. Swierk,[2] Coleen T. Nemes,[2] Charles A. Schmuttenmaer,[2,*] Thomas E. Mallouk[1,3,4,*]

[1]*Department of Chemistry,* [3]*Department of Biochemistry and Molecular Biology, and* [4]*Department of Physics, The Pennsylvania State University, University Park, Pennsylvania 16802 United States*

[2]*Department of Chemistry and Energy Sciences Institute, Yale University, 225 Prospect Street, P.O. Box 208107, New Haven, Connecticut, 06520-8107, United States*

Experimental

Bis(2,2′-bipyridine)(4,4′-diphosphonato-2,2′-bipyridine)ruthenium(II) bromide (Ru(II)phos) was prepared as previously described.[1]

Sample Preparation. SnO_2 pastes were prepared following the method of Ito et al.[2] Briefly, SnO_2 (Aldrich, 20-40 nm) was successively ground with acetic acid, water, and ethanol to give a suspension, which was ultrasonicated for 15 min. The suspension was allowed to sit for three hours to allow large aggregates to settle. After settling, α-terpineol was added with stirring, followed by an additional 10 min of ultrasonication. Finally, a 10 wt% solution of ethyl cellulose in ethanol was added with stirring, again followed by ultrasonication for 10 min. The ethanol was subsequently removed via rotary evaporation to give a paste.

Films were prepared doctor-blading on fused quartz substrates (GM Associates, Inc.) using Scotch Magic tape as a spacer layer. After each layer of paste was applied, the film was cured at 80 °C for 10 min before the next layer was applied. A total of three layers of paste were used for all samples, giving a final film thickness of 6 μm after sintering. The films were sintered using the following program: 3 °C/min to 370 °C, hold for 10 min, 3 °C/min to 470 °C, hold for 30 min, cool to room temperature.

Core/Shell structures were fabricated using a Cambridge Savannah 200 atomic layer deposition (ALD) system. Samples were loaded in to the deposition chamber and the chamber temperature was increased to the required temperature for the different materials followed by alternating pulses of water vapor and the respective metal oxide precursor. Due to the high surface area of the films, vapor pulses were held in the reaction chamber for 3 minutes followed by opening the valve and purging with N_2 for 25 seconds before the next pulse. TiO_2 was deposited as previously reported,[3] utilizing tetrakis(dimethylamido)titanium as the precursor and a deposition temperature of 150 °C and a precursor temperature of 75 °C. The pulse durations were 0.03 s and 0.25 s for the water vapor and TiO_2 precursor, respectively. These cycles were repeated for 1, 2, 5, 10, 20, and 40 iterations to make core/shell structures with varying thicknesses of shell material. Following shell deposition, all electrodes (including bare electrodes for comparability) were sintered a second time at 450 °C for 30 min before they were sensitized

with dye. All films were sensitized in the dark from a 100 μM solution of Ru(II)phos in anhydrous ethanol for 16 hours, rinsed with ethanol, and dried under a stream of nitrogen.

Samples for TRTS spectroscopy were sealed using a second piece of fused quartz, with a 1 mm hole previously drilled into it, with a 60 μm Surlyn (Solaronix) spacer between the two pieces of quartz. The pieces of quartz were hot pressed to bond to the Surlyn and 0.1 M $HClO_4$ introduced via vacuum backfilling. Finally, the hole filling hole was covered with a small square of Surlyn, covered with a 1 cm^2 glass coverslip, and heat sealed using a soldering iron.

Characterization. Fluorescence spectroscopy was done on a SPEX Fluorolog 2 double grating fluorometer with at 450 W Xenon lamp. Electrodes for fluorescence were fabricated as above with varying thicknesses of a TiO_2 a mesoporous film of SnO_2 or ZrO_2. The instrument was operated in front facing mode with the metal oxide film tilted 45° from the excitation beam and facing nearly directly at the fluorescence detector. Emission was detected through a 1.5 mm slit width at a photomultiplier tube that had been normalized to the response sensitivity of the detector across the various wavelengths collected. Fluorescence was carried out in a N_2 degassed pH 1, 0.1 M $HClO_4$ aqueous solution. The electrodes were all excited at 460 nm and emission was collected from 510 – 800 nm with a step size of 1 nm and integration time of 1 s at each step. Experimental conditions were identical between samples in order to make emission intensity comparable across all measured electrodes.

Scanning/transmission electron microscopy (S/TEM) and energy dispersive X-ray spectroscopy (EDS) was carried out on an FEI Talos F200X S/TEM instrument.

X-ray photoelectron spectroscopy (XPS) was carried out on a PHI *VersaProbe* II Scanning XPS Microprobe.

UV/Vis spectra were collected on a Cary 6000i UV-Vis-NIR spectrometer on dry films. The instrument was blanked to air and a zero light baseline was collected by blocking the beam. Spectra were collected from 800 to 200 nm, scanning at 10 nm/s with an interval of 1 nm. Surface coverage for Ru(II)phos was calculated using the same method as Hanson et al. at 453 nm, the peak absorption of this dye:[4]

$$\Gamma = \frac{A(\lambda)}{1000 * \varepsilon(\lambda) * t}$$

where A(λ) is the baseline corrected absorbance at 453 nm, ε(λ) is the molar absorptivity constant at 453 nm and t is the film thickness.

Time-resolved terahertz spectroscopy (TRTS) was carried out as described in detail elsewhere.[3,5–8] In sum, the 35 fs pulse of an amplified Ti:sapphire laser (Spectra Physics, 800 nm, 1kHz repetition) is split into three beams: pump, generation, and detection. The generation beam is used to generate terahertz (THz) radiation by frequency doubling to 400 nm, with both the fundamental and second harmonic focused in air to generate a plasma.[9,10] The forward propagating THz radiation generated by the plasma is collected and focused using off-axis paraboloidal mirrors, and is detected using free-space electro-optic sampling with a ZnTe(110) crystal.[11] Finally, the pump beam is frequency doubled to 400 nm and a variable neutral density filter used to adjust the power to 100 mW/cm^2 (6 mm diameter spot).

Results

Table S1. Fitting parameters from equation S1 for TRTS traces in Figure 2

Shell thickness (Å)	A_1 (%)	τ_1 (ps)	A_2 (%)	τ_2 (ps)	A_3 (%)	τ_3 (ps)	A_4 (%)	τ_4 (ps)	scaling factor*	$\langle\tau_w\rangle$ (ps)
0.63	0.48	2.8	0.45	17	0.07	154			1.57	20
0.63	0.37	2.1	0.50	11	0.13	47			1.31	12
1.26	0.43	3.4	0.43	18	0.14	111			1.32	25
1.26	0.26	2.0	0.49	9	0.25	51			1.63	18
3.15	0.44	5.36	0.41	30	0.19	201			1.11	52
3.15	0.30	3.1	0.45	22	0.25	151			1.16	48
6.30	0.13	<0.5	0.43	28	0.44	217			0.81	108
6.30	0.10	<0.5	0.47	24	0.43	213			1.07	102
12.6	0.09	<0.5	-0.03	0.59	0.42	41	0.48	300	0.64	163
12.6	0.07	<0.5	-0.04	1.1	0.42	71	0.51	348	0.80	207
25.2	0.16	<0.5	-0.15	1.1	0.60	78	0.24	356	0.63	133
25.2	0.30	<0.5	-0.18	0.6	0.42	54	0.11	340	0.40	118

*Scaling factor is the sum of all A components before normalization

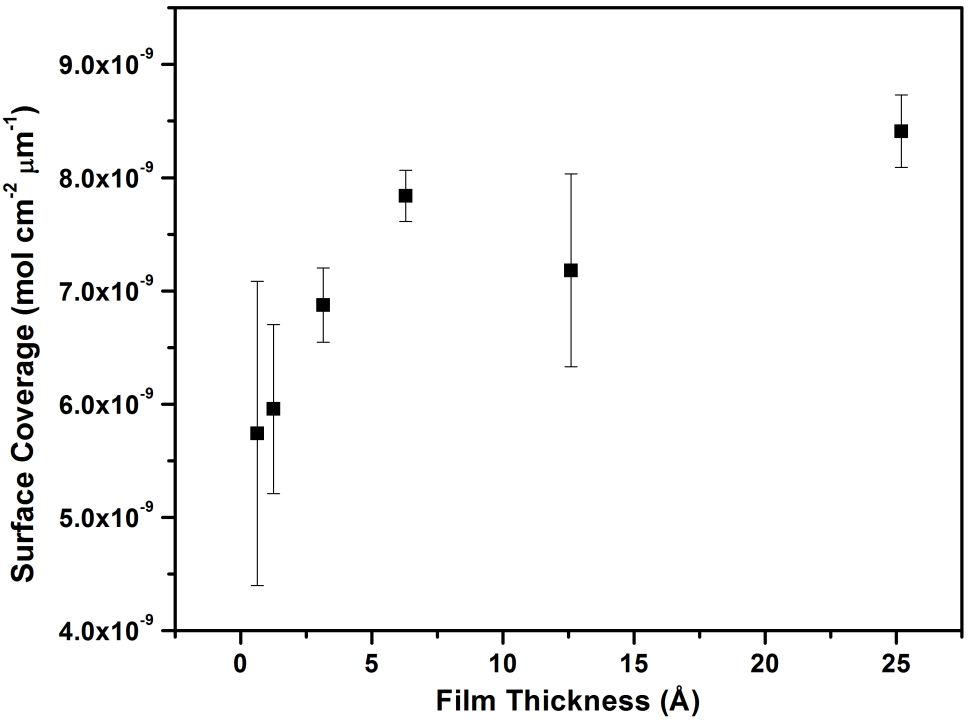

Figure S1. Surface coverage of Ru(II)phos on the surface of the SnO_2/TiO_2 electrodes with increasing thickness of the TiO_2 shell. Surface coverage calculated from the absorbance of dry films at 453 nm.

References

(1) Gillaizeau-Gauthier, I.; Odobel, F.; Alebbi, M.; Argazzi, R.; Costa, E.; Bignozzi, C. A.; Qu, P.; Meyer, G. J. Phosphonate-Based Bipyridine Dyes for Stable Photovoltaic Devices. *Inorg. Chem.* **2001**, *40* (23), 6073–6079.

(2) Ito, S.; Chen, P.; Comte, P.; Nazeeruddin, M. K.; Liska, P.; Péchy, P.; Grätzel, M. Fabrication of Screen-Printing Pastes from TiO_2 Powders for Dye-Sensitised Solar Cells. *Prog. Photovoltaics* **2007**, *15* (7), 603–612.

(3) Swierk, J. R.; McCool, N. S.; Nemes, C. T.; Mallouk, T. E.; Schmuttenmaer, C. A. Ultrafast Electron Injection Dynamics of Photoanodes for Water-Splitting Dye-Sensitized Photoelectrochemical Cells. *J. Phys. Chem. C* **2016**, *120* (11), 5940–5948.

(4) Hanson, K.; Brennaman, M. K.; Ito, A.; Luo, H.; Song, W.; Parker, K. A.; Ghosh, R.; Norris, M. R.; Glasson, C. R. K.; Concepcion, J. J.; et al. Structure–Property Relationships in Phosphonate-Derivatized, Ru II Polypyridyl Dyes on Metal Oxide Surfaces in an Aqueous Environment. *J. Phys. Chem. C* **2012**, *116* (28), 14837–14847.

(5) Beard, M. C.; Turner, G. M.; Schmuttenmaer, C. A. Transient Photoconductivity in GaAs as Measured by Time-Resolved Terahertz Spectroscopy. *Phys. Rev. B: Condens. Matter Mater. Phys.* **2000**, *62* (23), 15764–15777.

(6) Turner, G. M.; Beard, M. C.; Schmuttenmaer, C. A. Carrier Localization and Cooling in Dye-Sensitized Nanocrystalline Titanium Dioxide. *J. Phys. Chem. B* **2002**, *106* (45), 11716–11719.

(7) Baxter, J. B.; Schmuttenmaer, C. A. Conductivity of ZnO Nanowires, Nanoparticles, and Thin Films Using Time-Resolved Terahertz Spectroscopy. *J. Phys. Chem. B* **2006**, *110*

(50), 25229–25239.
(8) Nemes, C. T.; Koenigsmann, C.; Schmuttenmaer, C. A. Functioning Photoelectrochemical Devices Studied with Time-Resolved Terahertz Spectroscopy. *J. Phys. Chem. Lett.* **2015**, *6* (16), 3257–3262.
(9) Bartel, T.; Gaal, P.; Reimann, K.; Woerner, M.; Elsaesser, T. Generation of Single-Cycle THz Transients with High Electric-Field Amplitudes. *Opt. Lett.* **2005**, *30* (20), 2805–2807.
(10) Cook, D. J.; Hochstrasser, R. M. Intense Terahertz Pulses by Four-Wave Rectification in Air. *Opt. Lett.* **2000**, *25* (16), 1210–1212.
(11) Wu, Q.; Zhang, X. C. Free-Space Electro-Optic Sampling of Terahertz Beams. *Appl. Phys. Lett.* **1995**, *67* (1995), 3523–3525.